photonics

MDPI

Article

All-Metal Coding Metasurfaces for Broadband Terahertz RCS Reduction and Infrared Invisibility

Ming Zhang *, Najiao Zhang, Peng Dong, Lin Yang, Baozhu Wang, Ruihong Wu and Weimin Hou *

School of Information and Engineering, Hebei University of Science and Technology, Shijiazhuang 050018, China; zhangnajiao@stu.hebust.edu.cn (N.Z.); dongpeng5261@stu.hebust.edu.cn (P.D.); yanglin@hebust.edu.cn (L.Y.); wangbz@hebust.edu.cn (B.W.); wurh@hebust.edu.cn (R.W.)

* Correspondence: zhangming369@hebust.edu.cn (M.Z.); hwm@hebust.edu.cn (W.H.)

Abstract: With the rapid advancement of modern technology and radar detection systems, electromagnetic (EM) stealth technology has become increasingly significant, particularly in aircraft stealth and military radar applications. In this work, an all-metal metasurface is designed for broadband terahertz radar cross-section (RCS) reduction and infrared invisibility. The all-metal metasurface possesses extremely low infrared emissivity and high polarization conversion in the terahertz band. Through the joint simulation of MATLAB and CST, a genetic algorithm is used to optimize the random phase distribution of 2, 3, and 4-bit metasurfaces, so that the reflected wave is scattered to achieve broadband terahertz RCS reduction. Simulation results show that the metasurface can simultaneously achieve broadband terahertz RCS reduction in 3–5 THz and infrared invisibility in 24–38 THz (8–12.5 μm). The RCS reduction of the coding metasurface is greater than 10 dB compared to the metal plate, and the maximum RCS reduction of the 4-bit metasurface can reach 21.1 dB. Compared to the traditional design method, the proposed method can reduce time consumption and find the optimal result to achieve high performance. We believe the proposed method can provide significant guidance for surface coating in camouflage applications and opens up new possibilities for improving the information capacity of coding metasurfaces.

Keywords: broadband terahertz RCS reduction; coding metasurface; genetic algorithm

Citation: Zhang, M.; Zhang, N.; Dong, P.; Yang, L.; Wang, B.; Wu, R.; Hou, W. All-Metal Coding Metasurfaces for Broadband Terahertz RCS Reduction and Infrared Invisibility. *Photonics* **2023**, *10*, 962. https://doi.org/10.3390/photonics10090962

Received: 20 July 2023
Revised: 10 August 2023
Accepted: 16 August 2023
Published: 23 August 2023

1. Introduction

With the development of science and technology, the application range of EM wave technology has been expanding [1–3]. Regardless of the underlying mechanism of each application, all different applications are achieved on the basis of manipulating fundamental properties of EM phenomena during their propagation [4]. Recently, artificially structured metasurfaces have shown flexible manipulation of amplitude, phase, and polarization of EM waves [5–12]. Metasurfaces' exceptional properties and abilities have made breakthroughs in many different fields, including stealth technology [13–17], quantum photonics [18], optical devices [19,20], and even polarization transformation devices [21,22]. Among them, stealth technology is the most important technology for the development of military power under the condition of informational warfare [23–25]. Radar stealth is mainly achieved by redirecting the scattering wave to an abnormal direction to reduce the RCS of the target [26,27]. Infrared stealth is mainly in the wavelength range of 3–14 μm, and is achieved by reducing the infrared emissivity of the object's surface [28–30].

Recently, various building blocks are presented to construct metasurfaces for RCS reduction and infrared invisibility [31,32]. In 2019, Pedersen's team realized a structure in which a reflective antenna and a lens are coated on the absorbing material unit. Compared with the traditional reflective array antenna, wideband RCS reduction on checkerboard metasurfaces with dual resonance and surface wave suppression was implemented by Kim et al. in the same year [33]. The proposed structure increases the high frequency of the −10 dB RCS reduction from 14.9 to 16.32 GHz. At the same time, Xie et al. proposed a new

method of using a heat-resistant all-metal metasurface as a new thermal infrared stealth [34]. The designed metasurface has strong EM wave manipulation ability. In order to further improve the EM control ability of metasurfaces, the team of Cui proposed the concept of 'coding metamaterials', which can regulate electromagnetic waves by digital coding of units [35]. The digital coding metasurface is a new type of metasurface, which brings a fancy perspective on the connection between physics and information science [36–40]. In 2021, Cao's group presented a design method using simple patches with a non-resonant mode to achieve broadband phase-gradient metasurfaces of a reflective type [41]. A design example of a reflective RCS reduction structure with a −10 dB bandwidth of 5.3–18 GHz is given to prove the efficiency of the method. Qi et al. proposed a high-efficiency reflective-type coding metasurface using the PB phase concept in the same year. The designed metasurface structure can arbitrarily manipulate the scattering mode of terahertz waves and realize many novel functions [42]. However, most of the metasurface devices at home and abroad can only work in a single frequency band. The research on metasurfaces that can achieve stealth in dual-band remains to be developed.

In this paper, an all-metal metasurface is designed for broadband terahertz RCS reduction and infrared invisibility. Through the joint simulation of MATLAB and CST, a genetic algorithm is used to optimize the random phase distribution of 2, 3, and 4-bit metasurfaces. The coding metasurface is composed of 20 × 20 unit structures with a PB phase, and the PB phase is controlled by 2, 3, and 4-bit of coding elements. In the frequency range of 3–5 THz, the RCS reduction of the coding metasurface is greater than 10 dB compared to the metal plate, and the maximum RCS reduction of the 4-bit metasurface can reach 21.1 dB. By comparing the 2, 3, and 4-bit coding sequences, it is shown that the higher the randomness of the PB phase of the structure, the better the RCS reduction. At the same time, the designed metasurface has low emissivity in the infrared band and has a good infrared stealth function. This method opens up new possibilities for improving the information capacity of coding metasurfaces and paves the way for further research on terahertz radar and infrared stealth technology.

2. Materials and Methods

2.1. Methods of RCS Reduction

RCS represents the echo intensity generated by a target object when it is detected by a radar's transmitted EM waves. RCS reduction can be achieved by controlling the amount of EM energy reflected in various directions using the coding elements of a metasurface. Under normal incidence of a plane wave, the far-field pattern function of the coding metasurface can be expressed as follows:

$$f(\theta,\varphi) = f_e(\theta,\varphi)\sum_{m=1}^{N}\sum_{n=1}^{N}\exp\left\{-i\left\{\varphi(m,n) + kp\sin\theta\left[\left(m-\frac{1}{2}\right)\cos\varphi + \left(n-\frac{1}{2}\right)\sin\varphi\right]\right\}\right\} \quad (1)$$

In the given context, $f_e(\theta,\varphi)$ represents the far-field function of the unit structure, where θ and φ are the elevation angle and azimuth angle in any given direction, respectively. $\varphi(m,n)$ represents the reflection phase of the unit at (m,n) position. $k = 2\pi/\lambda$ denotes the propagation constant, where λ is the wavelength. Additionally, p signifies the period of the unit structure. The directivity function $Dir(\theta,\varphi)$ of the metasurface is expressed as

$$Dir(\theta,\varphi) = \frac{4\pi|f(\theta,\varphi)|^2}{\left(\int_0^{2\pi}\int_0^{\frac{\pi}{2}}|f(\theta,\varphi)|^2\sin\theta d\theta d\varphi\right)} \quad (2)$$

During the design process, the cross-polarization reflection of the unit structure remains relatively consistent across all coding elements. However, the PB phases of the structural units associated with different coding elements are different, resulting in different phase differences. The scattering characteristics of two basic unit structures with a phase difference of 180° can be eliminated. From Equations (1) and (2), it can be seen

that the scattering characteristics of metasurfaces can be controlled by different sequences of coding units. Therefore, the EM wave incident on the coding metasurface scatters in multiple directions within space by optimizing the coding sequence. It can achieve RCS reduction to the greatest extent.

2.2. Multi-Bit Coding Metasurface

Figure 1a illustrates the schematic diagram of the coding metasurface, which is comprised of a 20 × 20 array of elements. Each individual array element contains a basic unit structure represented by a multi-bit element. This multi-bit element is composed of '0' and '1' elements, and their distribution within the array is randomized. The unit structure diagram of the metasurface is shown in Figure 1b,c. The structure consists of a metal plate with a thickness of t = 0.5 μm and a C-shaped split ring with a height of h = 20 μm. The opening angle of the C-shaped split ring is 115°. Both the metal plate and the C-shaped split ring are made of copper, with a conductivity of 5.96 × 10^7 S/m. Other detailed parameters of the unit structure are included p = 60 μm, R_1 = 26 μm, and R_2 = 18 μm. The unit structure is simulated in CST with a frequency range of 3–5 THz. The boundary conditions in the x, y, and z directions are set as open. The background distances along the z direction (both the upper and lower z distance) are set as 300 μm. A circular polarized light is applied in the simulation. The results of the reflection are shown in Figure 1d. The black dot-line diagram represents the reflection of cross-polarization, and the red dot-line diagram represents the reflection of co-polarization. It can be seen from the figure that the cross-polarization reflection of the unit structure largely exceeds 87% in the frequency range of 3–5 THz, which has a high conversion efficiency. Meanwhile, the co-polarization efficiency is very low. This shows that the unit structure has good wavefront control ability.

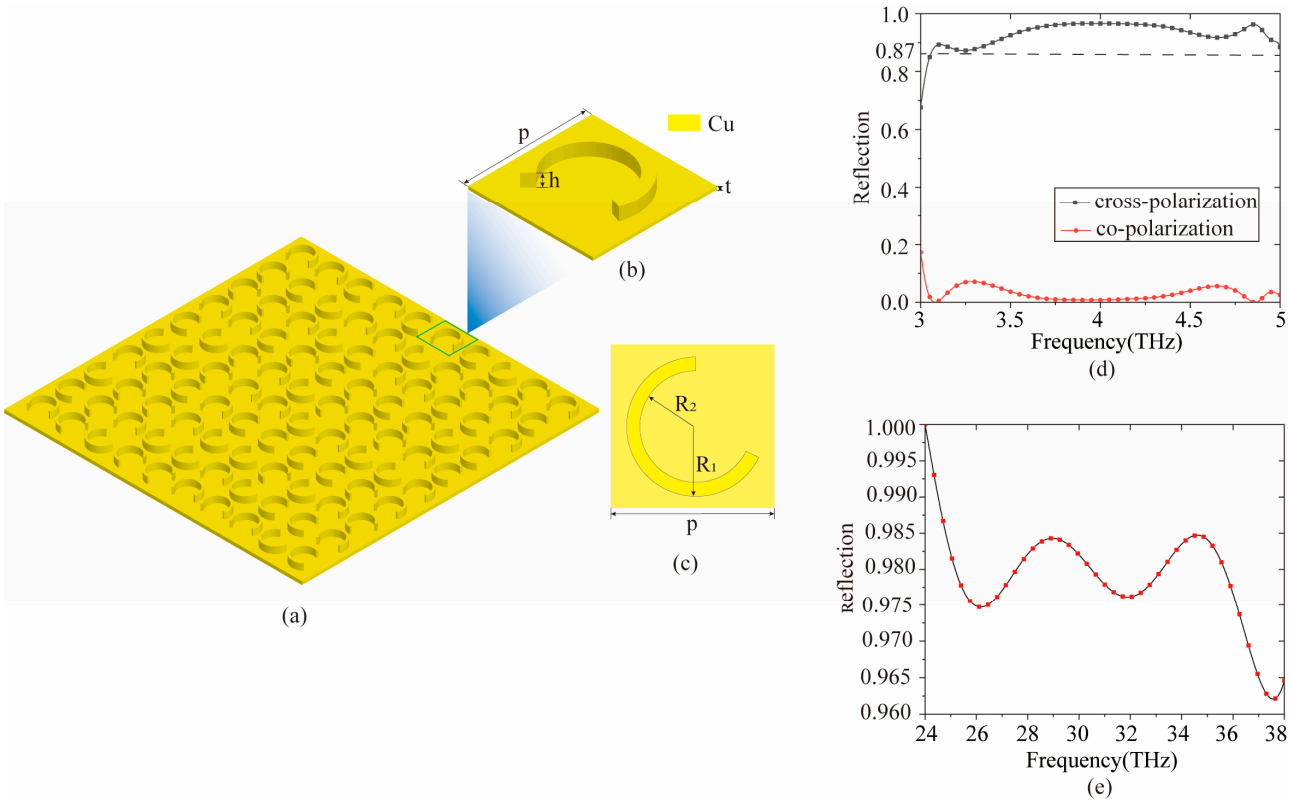

Figure 1. (**a**) Schematic of the proposed multi-bit coding metasurface. (**b**) The unit structure of the all-copper material. (**c**) The top view of the unit structure. (**d**) The cross-polarization and co-polarization reflection amplitude of the unit structure in the terahertz band. (**e**) The reflection amplitude distribution of the unit structure in the infrared band.

In addition, since the designed metasurface is composed of all-metallic materials, the structure also exhibits low infrared emission performance and can be used to wrap over an object to render it free from thermal infrared detection. This additional functionality is verified by CST simulation software. Other settings are consistent with the terahertz band, except for the frequency band. The unit structure is simulated in CST with a frequency range of 24–38 THz (8–12.5 μm). The result is shown in Figure 1e. The results demonstrate that the reflectivity of the structure exceeds 96% within the range of 24–38 THz. Because the metasurface has a metal substrate of sufficient thickness, its transmittance can be ignored. According to the principle of energy conservation, the sum of absorptivity, reflectivity, and transmittance is 100%. Therefore, the metasurface has a very low absorption in the infrared band. Based on Kirchhoff's law [43], low absorption represents low emissivity. The bandwidth of 24 to 38 THz is part of the atmospheric window of infrared radiation. The extremely low emissivity in this band means that the designed metasurface cannot be recognized by passive infrared monitoring equipment.

3. Results and Discussion

3.1. Design of Coding Metasurface

The electromagnetic wave modulation characteristics of coding metasurfaces are closely related to their phase distribution. The phase distribution of multi-bit coding metasurfaces is diverse. It is challenging to find the coding metasurface with the best scattering effect from these phase distributions, which requires researcher experience and a significant amount of time and effort. Therefore, we proposed a convenient and automatic design approach to optimize the phase distribution of the coding metasurface, which is achieved by joint simulation of CST and MATLAB. First, the parameters of the unit are continuously optimized to meet the requirements in CST. Then, the coding elements of different bits are obtained by changing the phase of the optimized unit. Finally, MATLAB is used to control the generation of random coding elements and simulate them in CST. The coding metasurface is composed of 20 × 20 unit structures, that is, its size is 1.2 mm × 1.2 mm. The frequency is set to 3–5 THz in the simulation. The boundary conditions in the x, y, and z directions are set as open (add space). The background distances along the z direction (both the upper and lower z distance) are set as 300 μm. We set up probes and far-field monitors to observe RCS results. Considering the actual test environment, linear polarized light is applied in the simulation. The whole process uses the genetic algorithm to optimize the coding sequence until the optimal solution is obtained. The genetic algorithm, first proposed by Professor John in 1992 [44], is a global optimization algorithm inspired by the natural evolution of organisms. It serves as a computational model that simulates Darwin's theory of biological evolution. The fundamental concept revolves around the principle of "survival of the fittest" where each generation strives to outperform the previous one. This is achieved through the basic processes of selection, crossover, and mutation. The selection method employed is tournament selection. The underlying principle is to choose a specific number of individuals from the population in each round. The individual with the highest fitness value is selected to enter the offspring population. This process is repeated multiple times to generate a new offspring population. For crossover, the simplest method, known as single-point crossover, is used. A random position is selected, and the information of the two parent individuals is swapped after that position. Mutation, on the other hand, involves randomly selecting a location and making random changes to the information at that location. We demonstrate the specific process in Figure 2a. By utilizing computer simulation and mathematical methods, the algorithm transforms the problem-solving process into a procedure resembling biological evolution. In the case of solving complex combinatorial optimization problems, the genetic algorithm often yields superior optimization results at a faster pace compared to conventional optimization algorithms.

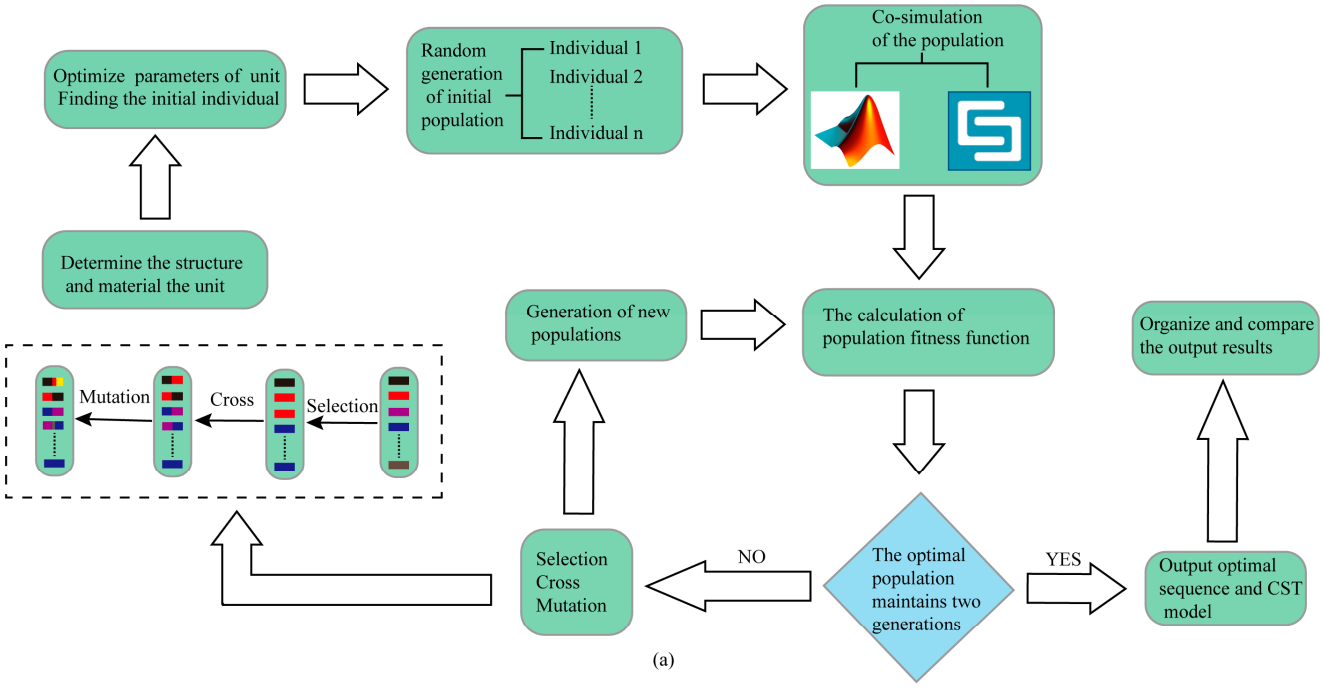

(a)

Phase and shape / Multi-bit	0	π/8	2π/8	3π/8	4π/8	5π/8	6π/8	7π/8	8π/8	9π/8	10π/8	11π/8	12π/8	13π/8	14π/8	15π/8
2-bit	00				01				10				11			
3-bit	000		001		010		011		100		101		110		111	
4-bit	0000	0001	0010	0011	0100	0101	0110	0111	1000	1001	1010	1011	1100	1101	1110	1111

(b)

Figure 2. (**a**) Flow chart of the whole design. (**b**) Coding elements corresponding to 2, 3, and 4-bit phases.

Figure 2a illustrates the flow chart of the whole design employed in this paper. The design concept of this randomly coding metasurface is as follows: firstly, an all-metal C-shaped split ring was proposed through optimization design and simulation. Secondly, the cross-polarization reflection phase within the range of 3–5 THz was selected as the reference. Next, the genetic algorithm was applied to optimize the coding matrix of the metasurface in order to obtain the optimal solution for diffuse scattering characteristics. Based on the aforementioned approach, the coding elements of different bits serve as the population for the genetic algorithm, with its diffusion characteristics used as the fitness. The coding elements are obtained by the geometric phase of the control unit, and the corresponding relationship is shown in Figure 2b. From Figure 2b, it is evident that 2-bit corresponds to 4 coding elements, 3-bit corresponds to 8 coding elements, and 4-bit corresponds to 16 coding elements. The phase of each bit's coding element ranges from 0 to 2π. Since the phase angle is twice the rotation angle, the rotation angle only needs to cover π. Based on the unit structure with a phase of 0, the unit structure corresponding to the current coding element is obtained by rotating the unit structure corresponding to the previous coding element by $\pi/16$.

The metasurface can be regarded as an $M \times N$ matrix, where M and N represent the number of units along the x-axis and y-axis, respectively. In the simulation, the values of M and N are both set to 20. To enhance the design of broadband RCS reduction devices,

the population size is set to 40, the crossover probability ranges from 0.7 to 0.9, and the mutation probability ranges from 0.001 to 0.05. Each population contains 20 individuals. The interval from −30 to −46 dB, with a −2 dB increment, is divided into 8 sub-intervals. Additionally, the frequency range of 3–5 THz is divided into 1001 frequency points. The frequency points within the RCS result interval are represented as N_1 to N_8. That is to say, the number of frequency points with RCS values from −30 to −32 dB is recorded as N_1, and the number of frequency points with RCS values from −32 to −34 dB is recorded as N_2, and so on, until N_8. The number of frequency points with RCS values less than −46 dB is recorded as N_9. The fitness function for the population is determined by obtaining the value of Equation (3).

$$\text{value} = N_1 \times 1 + N_2 \times 3 + N_3 \times 5 + N_4 \times 7 + N_5 \times 9 + N_6 \times 11 + N_7 \times 13 + N_8 \times 15 + N_9 \times 17 \quad (3)$$

The coefficient in Equation (3) represents the weight of N_i. We add different coefficients to N_i to obtain a reasonable fitness function. Reasonable fitness functions can improve the performance of genetic algorithms. The termination criteria for the population are based on the average fitness becoming equal to the maximum fitness and maintaining this consistency for two consecutive generations. If the condition is met, the coding sequence and RCS value associated with the optimal solution are outputted. On the contrary, the current population is abandoned and a new population is generated. The relevant parameters of the new population are calculated through the processes of selection, crossover, and mutation. This cycle continues until the optimal solution is found.

3.2. Simulation and Analysis of Coding Metasurface

To investigate the scattering characteristics of the metasurface, we conducted simulations using CST for five types of different metasurfaces at 4 THz, including the metal plate, a 4-bit random coding metasurface, and three 4-bit fixed coding metasurfaces. The simulation results are presented in Figure 3. Figure 3a shows the RCS results of five types of different metasurfaces, in which three different sequences of 4-bit fixed coding metasurfaces are designed to illustrate the following conclusion. From Figure 3a, we can see that the RCS of all fixed coding sequence metasurfaces is significantly lower than that of the metal plate, and the RSC reduction is above 5 dB. Compared with the fixed coding sequence, the RCS result of the random coding sequence metasurface is generally lower and the reduction is more obvious. Compared with the metal plate, the RCS reduction of the random coding metasurface is greater than 10 dB. The local schematic and phase distribution of each metasurface are shown in Figures 3b–f and 3g–k, respectively. The horizontal and vertical coordinates of the phase distribution diagram represent the *Nth* unit on the *x*-axis and the *y*-axis, respectively. It more vividly illustrates the specific structure of each metasurface. Since there is no structure on the metal plate, its phase distribution is 0. The phase distribution of the three 4-bit fixed coding metasurfaces is to arrange the sixteen coding elements of 4-bit from 0 to 2π, where each element is repeated once, twice, and three times, respectively. The phase distribution of the 4-bit random coding metasurface is optimized by a genetic algorithm.

We present three-dimensional scattering maps of the aforementioned five metasurfaces at 4 THz to gain a deeper understanding of the diffusion behavior. As shown in Figure 3l–p, we can observe distinct differences among the five structures. In the case of the metal plate, a clear main lobe is evident in the reflected wave. In 4-bit fixed coding metasurfaces, light is mainly scattered in several fixed directions, which has poor scattering characteristics. Obviously, in the case of the 4-bit random coding metasurface, there is almost no prominent main lobe in the reflected wave, and the energy in each beam direction is significantly reduced. The polar diagrams in Figure 3q–u provide a quantitative representation of the RCS reduction, which further illustrates the scattering characteristics. It can be seen from the diagram that the scattering direction of the metal plate is concentrated in the mirror direction, and the RCS is larger than the other four groups of data. The scattering direction of the 4-bit fixed coding metasurfaces begins to increase and the RCS decreases. The

4-bit random coding metasurface exhibits substantial suppression in all scattering levels, particularly in the mirror direction, when compared to other types of metasurfaces. At the same time, its RCS reaches the minimum. Based on these observations, we can conclude that the genetic algorithm-optimized coding metasurface demonstrates a more pronounced RCS reduction compared to the other metasurface types.

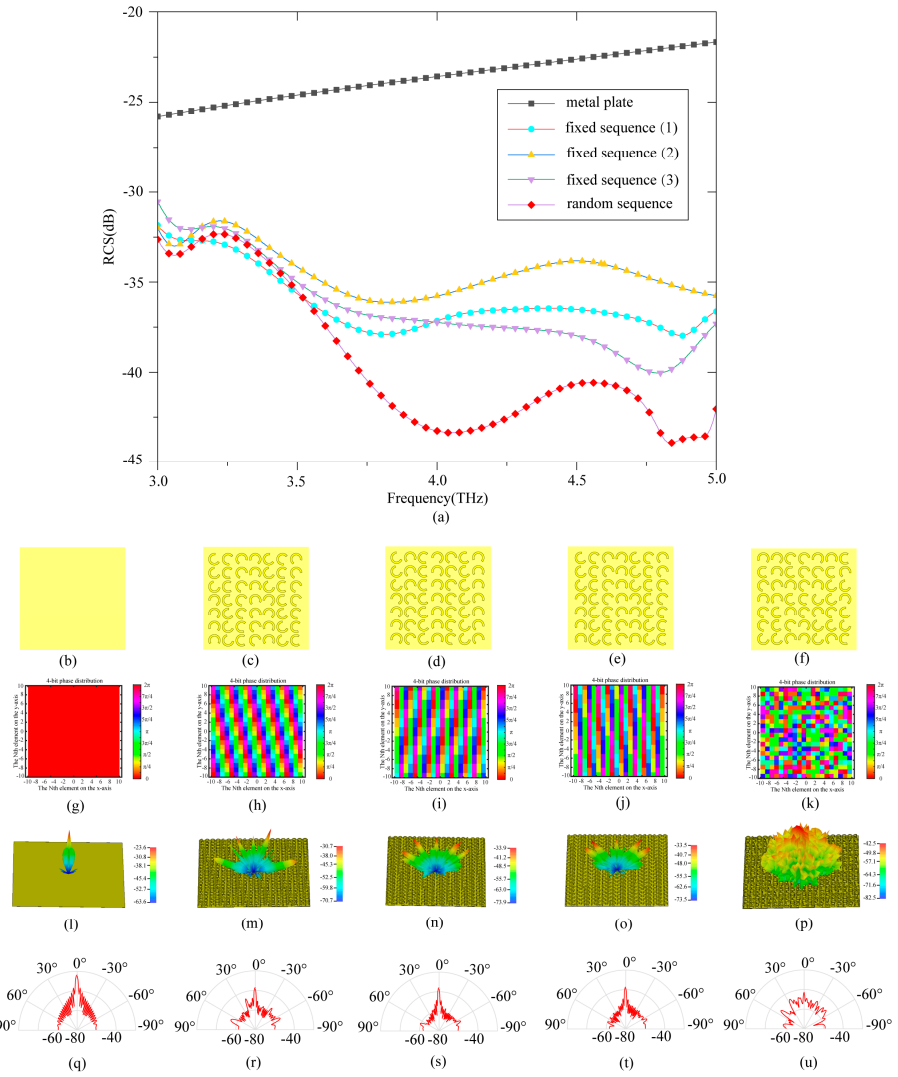

Figure 3. The simulation results of the metal plate, 4-bit fixed coding metasurfaces, and 4-bit random coding metasurface at 4 THz. (**a**) The RCS results of the above structure. (**b**–**f**) The structure diagram of the above structure. (**g**–**k**) The phase distribution of the above structure. (**l**–**p**) Three-dimensional scattering diagram of the above structure. (**q**–**u**) The polar diagram of the above structure.

Based on the above analysis, it can be concluded that the RCS reduction of the random phase distribution coding metasurface is superior to the fixed phase distribution. Therefore, we have conducted an optimization of the random phase arrangement for 2–4 bit coding metasurfaces. Due to the vast number of possible random phase distributions, it is challenging to manually find the coding metasurface with the best RCS reduction. This requires leveraging the joint simulation-based design method mentioned above and using genetic algorithms to obtain the optimal fitness function value for the random phase distribution, given the initial population. In the process of using a genetic algorithm to optimize the metasurface, the fitness curve fully proves the reliability of the results. For the optimal process, a server with an Intel(R) Core(M) CPU I9-10900X @3.70 GHz (10 cores, 20 threads) and 128 GB memory was employed. Figure 4a–c illustrate the evolutionary process of the

fitness function in the 2, 3, and 4-bit random coding metasurfaces. For the 2-bit coding metasurface, the optimal solution was achieved in the 9th generation. The 3-bit coding metasurface reached the optimal solution in the 10th generation. The 4-bit coding metasurface realized the optimal solution in the 8th generation. According to the result of running the program, the time consumption for the program to evolve one individual is 0.25 h; that is, the one-generation process only takes 5 h. It can be observed that the average fitness of the population gradually increases under the influence of the genetic algorithm. When the average fitness becomes equal to the maximum fitness and this fitness value is maintained for two consecutive generations, the program terminates. It guarantees the optimality and stability of the output results. Upon completion of the loop, the program generates a CST file containing the optimized metasurface structure and the corresponding RCS results. The phase distribution of the metasurface can be digitized and displayed more clearly by using the generated CST file. Figure 4d–f display the distribution of the metasurface coding matrix, which has been optimized using the genetic algorithm. The coding sequence of the metasurface is controlled by altering the PB phase of the unit structure through rotation.

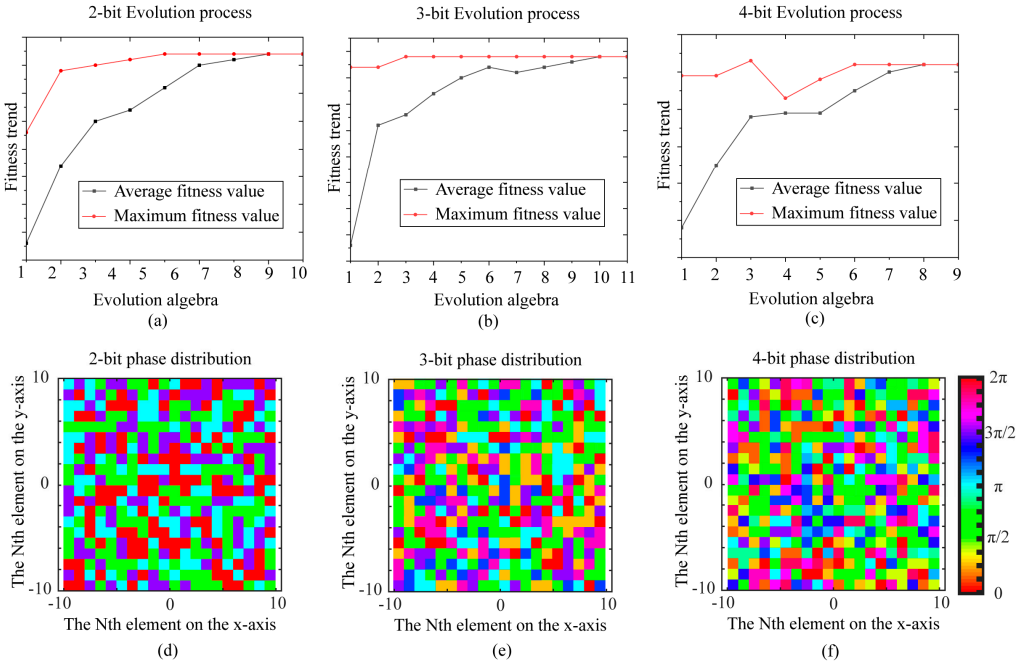

Figure 4. (**a**–**c**) The evolution process of 2, 3, and 4-bit random coding metasurfaces. (**d**–**f**) The phase distribution of 2, 3, and 4-bit random coding metasurfaces.

We designed the 2, 3, and 4-bit random coding metasurfaces and simulated and evaluated the RCS reduction and corresponding scattering effects, as depicted in Figure 5. It further illustrates the effectiveness of the proposed method. In Figure 5a, we observe that the RCS reduction of the 2, 3, and 4-bit random coding metasurfaces exceeds 10 dB compared to the metal plate, and the maximum RCS reduction of the 4-bit metasurface can reach 21.1 dB. Moreover, we note that the RCS of the 4-bit random coding metasurface is generally lower than that of the 3-bit metasurface, which, in turn, exhibits lower RCS than the 2-bit metasurface. Figure 5b,c show the local structure diagrams of the 2, 3, and 4-bit random coding metasurfaces. Moreover, Figure 5e–g also present the scattering maps at 4 THz for the 2, 3, and 4-bit random coding metasurfaces. In the three-dimensional scattering diagrams, the scattering level of the 2, 3, and 4-bit random coding metasurfaces is significantly limited. Furthermore, with the increase of bit, the scattering direction is more uniform. In particular, the scattering direction of 4-bit is significantly larger than that of 2-bit; multiple scattering beams are visible in the upper space. Figure 5h–j provide a more detailed illustration of the scattering characteristics of 2, 3, and 4-bit random coding metasurfaces. We can see that the scattering direction of the 2-bit random coding

metasurface is less than that of the other two, and the RCS is the largest. An increase in bit will lead to an increase in the scattering level of the metasurface and a decrease in RCS. This observation suggests that the RCS reduction improves as the number of bits in the coding matrix increases, along with the randomness of the coding sequence.

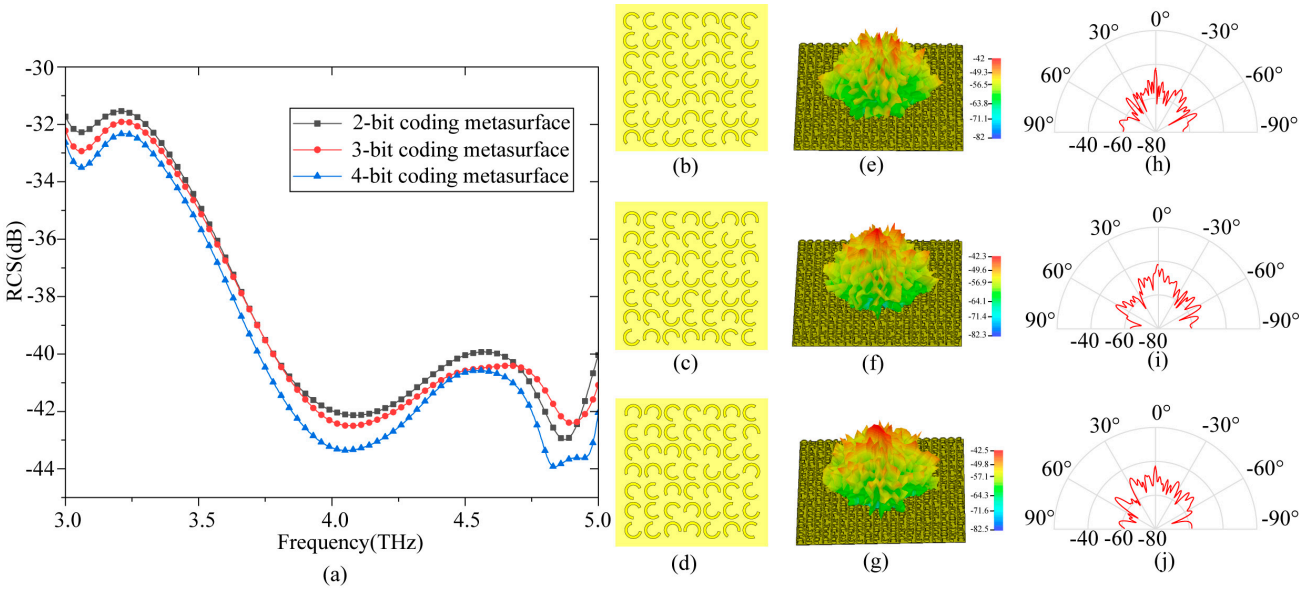

Figure 5. The simulation results of the 2, 3, and 4-bit coding metasurfaces at 4 THz. (**a**) RCS results of the above structure. (**b**–**d**) Schematic diagram of the above structure. (**e**–**g**) Three-dimensional scattering diagram of the above structure. (**h**–**j**) The polar diagram of the above structure.

We conducted the simulations to investigate the scattering patterns of 4-bit coding metasurfaces at different frequency points to illustrate the broadband capability of RCS reduction. Figure 6 presents the three-dimensional scattering diagrams, showcasing the reflection of incident waves in various directions at different frequencies. This phenomenon leads to the emergence of numerous side lobes with reduced energy, resulting in significant scattering suppression. Additionally, the polar diagrams in Figure 6 provide a quantitative description of the scattering characteristics at different frequency points. This representation effectively demonstrates the broadband stability of the metasurface's RCS reduction, illustrating its capability to reduce scattering over a wide frequency range. Moreover, the diffusion behavior of the scattering field can be clearly observed over this wide frequency range, emphasizing the metasurface's ability to mitigate scattering in diverse directions. Consequently, the designed random coding metasurface exhibits excellent RCS reduction effects across a broad frequency band.

In order to further characterize the broadband performance of the random coding metasurface, this work is compared with some previous works in the working frequency band. The comparison is shown in Table 1. We can see from Table 1 that the frequency range of this article is 2 THz, while the frequency range of other references does not exceed 1 THz. The relative bandwidth reaches 50%, and this parameter can be further enhanced by optimizing the unit structure to expand the operating frequency range in low frequency. The minimum RCS reduction of the designed coding metasurface is greater than 10 dB in the whole frequency band, and the maximum RCS reduction can reach 21 dB. The characterizations demonstrate the broadband feature of coding metasurfaces designed by co-simulation with a genetic algorithm.

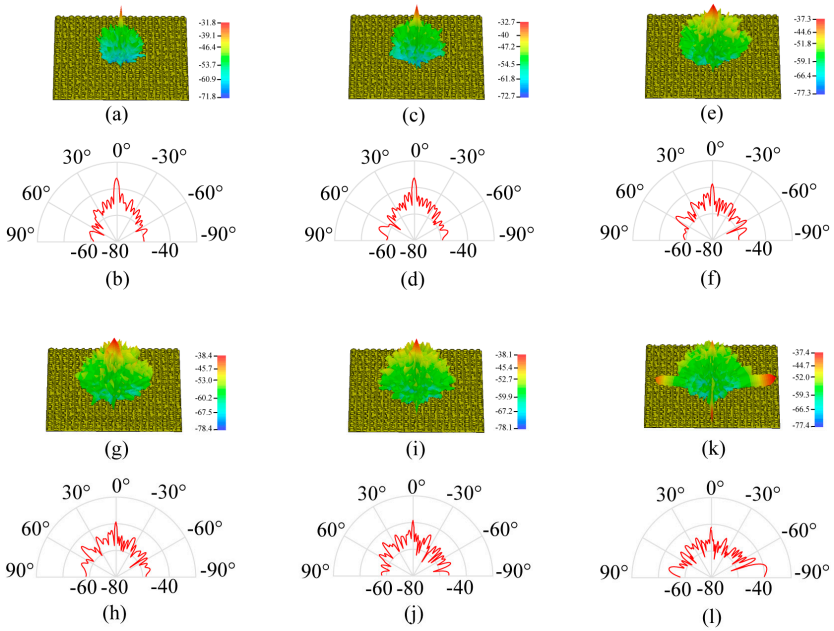

Figure 6. Three-dimensional scattering and polar diagram of different frequency points. (**a**,**b**) 3 THz. (**c**,**d**) 3.4 THz. (**e**,**f**) 3.8 THz. (**g**,**h**) 4.2 THz. (**i**,**j**) 4.6 THz. (**k**,**l**) 5 THz.

Table 1. Comparison with other references.

References	Frequency Range (THz)	Relative Bandwidth	RCS Reduction
Liang [45]	0.7–1.3	60%	18 dB (max)
Li [46]	0.7–1.45	70%	27 dB (max)
Zhang [47]	1.0–1.2	18%	13 dB (max)
Li [48]	0.6–1.6	91%	29 dB (max)
Zhou [49]	1.2–2.3	63%	20 dB (max)
This work	3–5	50%	21 dB (max)

The above results are obtained at specular reflection directions. Then, we discuss the output spectra under oblique incidence at 4 THz. The RCS reductions in the observation angles of 0°, 20°, 40° and 60° at 4 THz are plotted in Figure 7a. We can clearly observe scattering dips when the observation angles equal the incident angles (i.e., the specular reflection directions). The scattered fields at the other observation angles are still small, which confirms the excellent scattering behavior. From the scattering diagram of Figure 7b–i, the specular reflection is smaller than that of other observation angles, and the RCS reductions at all directions are larger than 10 dB. The above results confirm that our metasurface has great RCS suppression properties in wide incidence angles. In this design, the height of the split ring resonator is 20 μm and the feature size of the pattern is 8 μm, which makes the fabrication of the multifunctional coding metasurface difficult. Due to the limitations of fabrication and testing conditions, the coding metasurface has not been fabricated. However, we can provide a feasible fabrication plan here. The pattern of the metasurface can be achieved using mask lithography on the scale of a micrometer. Considering that the thickness of the unit structure is too large, the metal structure cannot be obtained through IBE etching after lithography. We can first fabricate the split ring resonator of silicon. The silicon split ring resonator can be fabricated combined with mask lithography and ICP etching to obtain a height of nearly 20 μm. Then, the sample is coated with a layer of copper seed for the electroplating process, and a layer of copper is electroplated above the silicon structure. Finally, we can obtain the all-metal multifunctional coding metasurface.

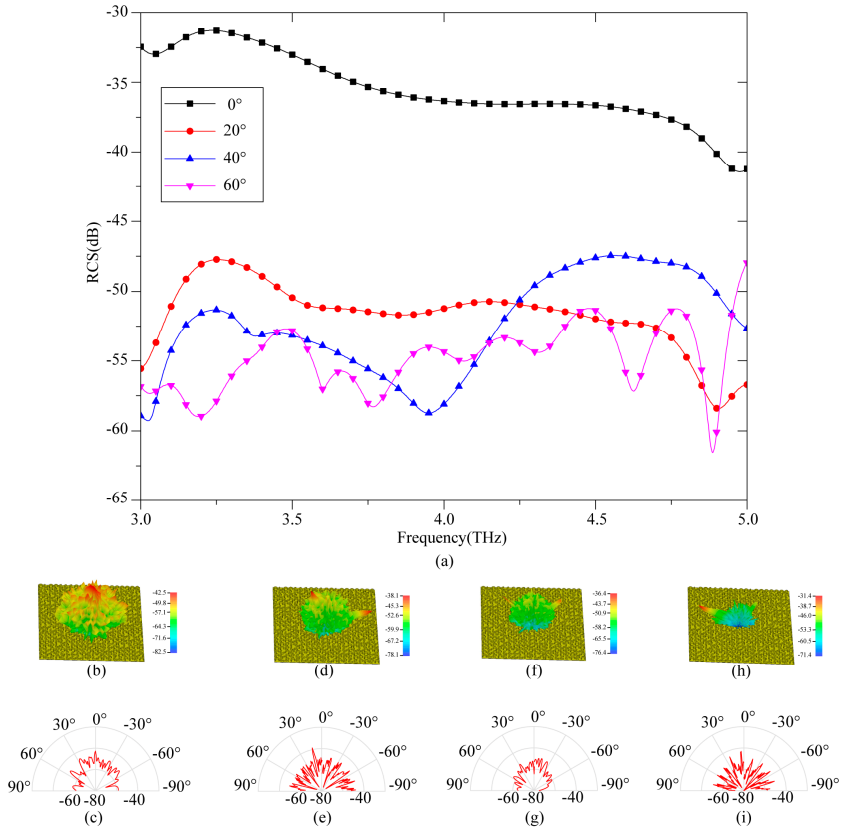

Figure 7. The output spectra under oblique incidence EM waves at 4 THz. (**a**) RCS results at different incident angles. (**b**,**c**) The scattering diagram when the incident angle is 0°. (**d**,**e**) The scattering diagram when the incident angle is 20°. (**f**,**g**) The scattering diagram when the incident angle is 40°. (**h**,**i**) The scattering diagram when the incident angle is 60°.

4. Conclusions

This work presents the design of an all-metal metasurface based on the theory of coding metasurfaces, aiming to achieve broadband terahertz RCS reduction and infrared invisibility. A genetic algorithm is used to optimize the coding sequence of random metasurfaces through the joint simulation of MATLAB and CST. The high performance and short design time of the metasurface are realized compared with the traditional metasurface design method. In this paper, 2, 3, and 4-bit coding metasurfaces are designed by using the above method. In the frequency range of 3–5 THz, simulation results demonstrate that the RCS reduction of the coding metasurface is greater than 10 dB when compared to the metal plate, and the maximum RCS reduction of the 4-bit metasurface can reach 21.1 dB. Comparative analysis of the 2, 3, and 4-bit coding sequences reveals that higher randomness in the PB phase of the structure leads to improved RCS reductions. Furthermore, the proposed unit structure exhibits low emissivity in the infrared band, rendering it effective for infrared stealth applications. This method opens up new possibilities for improving the information capacity of coding metasurfaces and paves the way for further research on cross-band stealth technology. We believe the proposed method can provide significant guidance for surface coating in conformal camouflage applications.

Author Contributions: Conceptualization, M.Z.; methodology, M.Z.; software, N.Z.; validation, N.Z. and P.D.; formal analysis, L.Y.; investigation, N.Z.; resources, L.Y.; data curation, R.W.; writing—original draft preparation, N.Z.; writing—review and editing, M.Z., B.W. and W.H.; visualization, R.W.; supervision, M.Z.; project administration, W.H.; funding acquisition, M.Z. All authors have read and agreed to the published version of the manuscript.

Funding: This research was funded by the National Natural Science Foundation of China (No. 62105093), the Science and Technology Project of Hebei Education Department (No. BJK2023036), and the Doctoral Research Initializing Fund of Hebei University of Science and Technology (No. 1181382).

Institutional Review Board Statement: Not applicable.

Informed Consent Statement: Not applicable.

Data Availability Statement: Data underlying the results presented in this paper are not publicly available at this time, but may be obtained from the authors upon reasonable request.

Conflicts of Interest: The authors declare no conflict of interest. The funders had no role in the design of the study; in the collection, analyses, or interpretation of data; in the writing of the manuscript; or in the decision to publish the results.

References

1. Xu, P.; Tian, H.W.; Cai, X.; Jiang, W.X.; Cui, T.J. Radiation-Type Metasurfaces for Advanced Electromagnetic Manipulation. *Adv. Funct. Mater.* **2021**, *31*, 2100569. [CrossRef]
2. Hestenes, D. Space-time structure of weak and electromagnetic interactions. *Found. Phys.* **1982**, *12*, 153–168. [CrossRef]
3. Li, X.F.; Liu, C.; Zhou, F.; Chen, Z.C.; Iraklis, G.; Evert, S. Deep learning–based nondestructive evaluation of reinforcement bars using ground-penetrating radar and electromagnetic induction data. *Comput.–Aided Civ. Infrastruct. Eng.* **2022**, *37*, 1834–1853. [CrossRef]
4. Zhang, L.; Mei, S.; Huang, K.; Qiu, C.-W. Advances in Full Control of Electromagnetic Waves with Metasurfaces. *Adv. Opt. Mater.* **2016**, *4*, 818–833. [CrossRef]
5. Li, Y.; Shen, C.; Xie, Y.; Li, J.; Wang, W.; Cummer, S.A.; Jing, Y. Tunable Asymmetric Transmission via Lossy Acoustic Metasurfaces. *Phys. Rev. Lett.* **2017**, *119*, 035501. [CrossRef]
6. Pendry, J.B.; Schurig, D.; Smith, D.R. Controlling Electromagnetic Fields. *Science* **2006**, *312*, 1780–1782. [CrossRef]
7. Schurig, D.; Mock, J.J.; Justice, B.J.; Cummer, S.A.; Pendry, J.B.; Starr, A.F.; Smith, D.R. Metamaterial Electromagnetic Cloak at Microwave Frequencies. *Science* **2006**, *314*, 977–980. [CrossRef]
8. Cheng, Q.; Jiang, W.X.; Cui, T.J. Spatial Power Combination for Omnidirectional Radiation via Anisotropic Metamaterials. *Phys. Rev. Lett.* **2012**, *108*, 213903. [CrossRef]
9. Guo, Y.; Yan, J.; Pu, M.; Li, X.; Ma, X.; Zhao, Z.; Luo, X. Ultra-wideband manipulation of electromagnetic waves by bilayer scattering engineered gradient metasurface. *RSC Adv.* **2018**, *8*, 13061–13066. [CrossRef] [PubMed]
10. Huang, Y.; Luo, J.; Pu, M.; Guo, Y.; Zhao, Z.; Ma, X.; Li, X.; Luo, X. Catenary Electromagnetics for Ultra-Broadband Lightweight Absorbers and Large-Scale Flat Antennas. *Adv. Sci.* **2019**, *6*, 1801691. [CrossRef]
11. Huang, Y.; Xiao, T.; Chen, S.; Xie, Z.; Zheng, J.; Zhu, J.; Su, Y.; Chen, W.; Liu, K.; Tang, M.; et al. All-optical controlled-NOT logic gate achieving directional asymmetric transmission based on metasurface doublet. *Opto-Electron. Adv.* **2023**, *6*, 220073. [CrossRef]
12. Tang, Z.; Li, L.; Zhang, H.; Yang, J.; Hu, J.; Lu, X.; Hu, Y.; Qi, S.; Liu, K.; Tian, M.; et al. Multifunctional Janus metasurfaces achieving arbitrary wavefront manipulation at dual frequency. *Mater. Des.* **2022**, *223*, 111264. [CrossRef]
13. Xu, H.-X.; Ma, S.; Ling, X.; Zhang, X.-K.; Tang, S.; Cai, T.; Sun, S.; He, Q.; Zhou, L. Deterministic Approach to Achieve Broadband Polarization-Independent Diffusive Scatterings Based on Metasurfaces. *ACS Photonics* **2017**, *5*, 1691–1702. [CrossRef]
14. Zhu, H.; Li, Q.; Tao, C.; Hong, Y.; Xu, Z.; Shen, W.; Kaur, S.; Ghosh, P.; Qiu, M. Multispectral camouflage for infrared, visible, lasers and microwave with radiative cooling. *Nat. Commun.* **2021**, *12*, 1805. [CrossRef] [PubMed]
15. Bilal, R.M.H.; Naveed, M.A.; Baqir, M.A.; Ali, M.M.; Rahim, A.A. Design of a wideband terahertz metamaterial absorber based on Pythagorean-tree fractal geometry. *Opt. Mater. Express* **2020**, *10*, 3007–3020. [CrossRef]
16. Naveed, M.A.; Bilal, R.M.; Rahim, A.A.; Baqir, M.A.; Ali, M.M. Polarization-insensitive dual-wideband fractal meta-absorber for terahertz applications. *Appl. Opt.* **2021**, *60*, 9160–9166. [CrossRef]
17. Yin, W.; Shen, Z.; Li, S.; Gao, F.; Hao, H.; Zhang, L.; Chen, X. Flexible broadband terahertz absorbers for RCS reduction on conformal surfaces. *Opt. Commun.* **2022**, *520*, 128502. [CrossRef]
18. Chen, Z.; Segev, M. Highlighting photonics: Looking into the next decade. *eLight* **2021**, *1*, 2. [CrossRef]
19. Song, S.; Ma, X.; Pu, M.; Li, X.; Guo, Y.; Gao, P.; Luo, X. Tailoring active color rendering and multiband photodetection in a vanadium-dioxide-based metamaterial absorber. *Photonics Res.* **2018**, *6*, 492–497. [CrossRef]
20. Sun, Z.; Yan, M.; Eric Mupona, T.; Xu, B. Control Electromagnetic Waves Based on Multi-Layered Transparent Metasurface. *Front. Phys.* **2019**, *7*, 181. [CrossRef]
21. Fu, C.; Sun, Z.; Han, L.; Liu, C. Dual-Bandwidth Linear Polarization Converter Based on Anisotropic Metasurface. *IEEE Photonics J.* **2020**, *12*, 2962336. [CrossRef]
22. Jia, M.; Wang, Z.; Li, H.; Wang, X.; Luo, W.; Sun, S.; Zhang, Y.; He, Q.; Zhou, L. Efficient manipulations of circularly polarized terahertz waves with transmissive metasurfaces. *Light Sci. Appl.* **2019**, *8*, 16. [CrossRef]
23. Pang, Y.; Shen, Y.; Li, Y.; Wang, J.; Xu, Z.; Qu, S. Water-based metamaterial absorbers for optical transparency and broadband microwave absorption. *J. Appl. Phys.* **2018**, *123*, 155106. [CrossRef]

24. Qi, D.; Wang, X.; Cheng, Y.; Gong, R.; Li, B. Design and characterization of one-dimensional photonic crystals based on ZnS/Ge for infrared-visible compatible stealth applications. *Opt. Mater.* **2016**, *62*, 52–56. [CrossRef]
25. Xu, C.; Wang, B.; Pang, Y.; Wang, J.; Yan, M.; Wang, W.; Wang, A.; Jiang, J.; Qu, S. Hybrid Metasurfaces for Infrared-Multiband Radar Stealth-Compatible Materials Applications. *IEEE Access* **2019**, *7*, 147586–147595. [CrossRef]
26. Fu, C.; Han, L.; Liu, C.; Lu, X.; Sun, Z. Combining Pancharatnam–Berry Phase and Conformal Coding Metasurface for Dual-Band RCS Reduction. *IEEE Trans. Antennas Propag.* **2022**, *70*, 2352–2357. [CrossRef]
27. Liu, X.; Gao, J.; Xu, L.; Cao, X.; Zhao, Y.; Li, S. A Coding Diffuse Metasurface for RCS Reduction. *IEEE Antennas Wirel. Propag. Lett.* **2017**, *16*, 724–727. [CrossRef]
28. Jiang, X.; Zhang, Z.; Ma, H.; Du, T.; Luo, M.; Liu, D.; Yang, J. Tunable mid-infrared selective emitter based on inverse design metasurface for infrared stealth with thermal management. *Opt. Express* **2022**, *30*, 18250–18263. [CrossRef] [PubMed]
29. Liu, B.; Shi, J.M.; Zhang, J.K.; Li, Z.G.; Chen, Z.S.; Deng, X.S. Infrared stealth performance analysis of photonic crystal with high heat dissipation. *Opt. Mater.* **2021**, *111*, 110689. [CrossRef]
30. Zhou, Y.-C.; Yang, J.; Bai, L.; Bao, R.-Y.; Yang, M.-B.; Yang, W. Flexible phase change hydrogels for mid-/low-temperature infrared stealth. *Chem. Eng. J.* **2022**, *446*, 137463. [CrossRef]
31. Mei, P.; Zhang, S.; Cai, Y.; Lin, X.Q.; Pedersen, G.F. A Reflectarray Antenna Designed With Gain Filtering and Low-RCS Properties. *IEEE Trans. Antennas Propag.* **2019**, *67*, 5362–5371. [CrossRef]
32. Huang, Q.; Zhao, Y.; Wu, Y.; Zhou, M.; Tan, S.; Tang, S.; Ji, G. A dual-band transceiver with excellent heat insulation property for microwave absorption and low infrared emissivity compatibility. *Chem. Eng. J.* **2022**, *446*, 137279. [CrossRef]
33. Kim, S.H.; Yoon, Y.J. Wideband Radar Cross-Section Reduction on Checkerboard Metasurfaces With Surface Wave Suppression. *IEEE Antennas Wirel. Propag. Lett.* **2019**, *18*, 896–900. [CrossRef]
34. Xie, X.; Pu, M.; Huang, Y.; Ma, X.; Li, X.; Guo, Y.; Luo, X. Heat Resisting Metallic Meta-Skin for Simultaneous Microwave Broadband Scattering and Infrared Invisibility Based on Catenary Optical Field. *Adv. Mater. Technol.* **2019**, *4*, 1800612. [CrossRef]
35. Cui, T.J.; Qi, M.Q.; Wan, X.; Zhao, J.; Cheng, Q. Coding metamaterials, digital metamaterials and programmable metamaterials. *Light Sci. Appl.* **2014**, *3*, e218. [CrossRef]
36. Bai, G.D.; Ma, Q.; Iqbal, S.; Bao, L.; Jing, H.B.; Zhang, L.; Wu, H.T.; Wu, R.Y.; Zhang, H.C.; Yang, C.; et al. Multitasking Shared Aperture Enabled with Multiband Digital Coding Metasurface. *Adv. Opt. Mater.* **2018**, *6*, 1800657. [CrossRef]
37. Gao, L.-H.; Cheng, Q.; Yang, J.; Ma, S.-J.; Zhao, J.; Liu, S.; Chen, H.-B.; He, Q.; Jiang, W.-X.; Ma, H.-F.; et al. Broadband diffusion of terahertz waves by multi-bit coding metasurfaces. *Light Sci. Appl.* **2015**, *4*, e234. [CrossRef]
38. Li, L.L.; Cui, T.J.; Ji, W.; Liu, S.; Ding, J.; Wan, X.; Li, Y.B.; Jiang, M.H.; Qiu, C.W.; Zhang, S. Electromagnetic reprogrammable coding-metasurface holograms. *Nat. Commun.* **2017**, *8*, 197. [CrossRef]
39. Liu, S.; Cui, T.; Zhang, L.; Xu, Q.; Wang, Q.; Wan, X.; Gu, J.; Tang, W.; Qi, M.; Han, J.; et al. Convolution Operations on Coding Metasurface to Reach Flexible and Continuous Controls of Terahertz. *Adv. Sci.* **2016**, *3*, 1600156. [CrossRef]
40. Liu, S.; Zhang, L.; Yang, Q.L.; Xu, Q.; Yang, Y.; Noor, A.; Zhang, Q.; Iqbal, S.; Wan, X.; Tian, Z.; et al. Frequency-Dependent Dual-Functional Coding Metasurfaces at Terahertz Frequencies. *Adv. Opt. Mater.* **2016**, *4*, 1965–1973. [CrossRef]
41. Wang, Y.; Chen, K.; Li, Y.; Cao, Q. Design of Nonresonant Metasurfaces for Broadband RCS Reduction. *IEEE Antennas Wirel. Propag. Lett.* **2021**, *20*, 346–350. [CrossRef]
42. Qi, Y.; Zhang, B.; Ding, J.; Zhang, T.; Wang, X.; Yi, Z. Efficient manipulation of terahertz waves by multi-bit coding metasurfaces and further applications of such metasurfaces. *Chin. Phys. B* **2021**, *30*, 024211.
43. Salisbury, J.W.; Wald, A.; D'Aria, D.M. Thermal-infrared remote sensing and Kirchhoff's law: 1. Laboratory measurements. *J. Geophys. Res. Solid Earth* **1994**, *99*, 11897–11911. [CrossRef]
44. Holland, J.H. Genetic algorithms. *Sci. Am.* **1992**, *267*, 66–73. [CrossRef]
45. Liang, L.; Wei, M.; Yan, X.; Wei, D.; Liang, D.; Han, J.; Ding, X.; Zhang, G.; Yao, J. Broadband and wide-angle RCS reduction using a 2-bit coding ultrathin metasurface at terahertz frequencies. *Sci. Rep.* **2016**, *6*, 39252. [CrossRef] [PubMed]
46. Li, S.; Li, J. Manipulating terahertz wave and reducing radar cross section (RCS) by combining a Pancharatnam–Berry phase with a coding metasurface. *Laser Phys.* **2019**, *29*, 075403. [CrossRef]
47. Zhang, H.; Huang, J.; Tian, M.; Liu, M.; Zhang, Y. 3-bit switchable terahertz coding metasurface based on Dirac semimetals. *Opt. Commun.* **2023**, *527*, 128958. [CrossRef]
48. Jiu-sheng, L.; Shao-he, L.; Jian-quan, Y. Actively tunable terahertz coding metasurfaces. *Opt. Commun.* **2020**, *461*, 125186. [CrossRef]
49. Zhou, C.; Peng, X.-Q.; Li, J.-S. Graphene-embedded coding metasurface for dynamic terahertz manipulation. *Optik* **2020**, *216*, 164937. [CrossRef]